Journal of Hazardous Materials 403 (2021) 124058

Contents lists available at ScienceDirect

Journal of Hazardous Materials

journal homepage: www.elsevier.com/locate/jhazmat

Mineralogical phase transformation of Fe containing sphalerite at acidic environments in the presence of Cu^{2+}

Yisheng Zhang [a,b], Hongbo Zhao [a,b,*], Xiaoyu Meng [a,b], Pengfei Ou [c], Xin Lv [a,b], Luyuan Zhang [a,b], Lixin Liu [d], Fashang Chen [d], Guanzhou Qiu [a,b]

[a] School of Minerals Processing & Bioengineering, Central South University, Changsha, Hunan, China
[b] Key Lab of Biohydrometallurgy of Ministry of Education, Changsha, Hunan, China
[c] Department of Mining and Materials Engineering, McGill University, Montreal, Quebec, Canada
[d] Jiangxi Sanhe Gold Co., Ltd., Jiangxi Province Engineering Research Center for Comprehensive Utilization of Refractory Gold Resources, China

ARTICLE INFO

Keywords:
AMD
pH values
Phase transition
Chalcopyrite
DFT calculations

ABSTRACT

Dissolution of the exposed sphalerite (marmatite) in abandoned mining sites and tailings may exacerbate acid and metalliferous drainage (AMD) hazards. Cupric ions are inevitable ions in AMD systems but its action mechanism on the dissolution of sphalerite is still unclear. In this work, the possible phase transition from sphalerite to chalcopyrite is firstly discovered in acidic cupric ions solution according to the results of Raman and (synchrotron radiation-based) X-ray (micro-) diffractometer spectra, which should be an important reason that mediates the dissolution of sphalerite. Results of DFT calculations reveal the underlying mechanism that Cu^{2+} can selectively replace zinc in marmatite lattices and further diffuse into the matrix. Additionally, a strong correlation between the cupric ion consumption with the pH value variation is discussed and the effects of the formed new phase on the dissolution kinetics of marmatite were researched. According to this work, the action mechanism of cupric ions on sphalerite dissolution in acidic environments is furtherly clarified.

1. Introduction

Mining is a strong support for human development, but its damage to the natural environment has also become a problem that must be solved for the progress of human society (Mehta et al., 2020; Ogbughalu et al., 2020). Acid and metalliferous drainage (AMD) is one of the most important concerns, which mainly occurs at the abandoned mine and smelting sites due to the oxidative dissolution of the exposed sulfide minerals (Sánchez-Andrea et al., 2014; Simate and Ndlovu, 2014). Prevention and treatment are the common AMD management approaches. The former aims to implement source control, including preventing the migration of AMD, averting the external water sources flowing/infiltration/seepage into the contaminated areas, and managing acid-generating waste. The latter is various, including physical remediation techniques (e.g. acid extraction, soil washing, encapsulation, dilution, and removal of polluted soil), chemical processes (e.g. lime neutralization/precipitation, cement neutralization), and biological approaches (e.g. phytoremediation, natural or man-made wetlands), etc (Akcil and Koldas, 2006; Sephton and Webb, 2019; Simate and Ndlovu, 2014; Wetle et al., 2020). However, different methods require varying degrees of financial support and have various shortcomings, such as inefficient for large sites, not entirely remove contaminants, and causing the loss of nutrients in the soil (Jin et al., 2020; Wetle et al., 2020). Therefore, understanding the internal behavior mechanism of minerals in AMD can provide a great reference for the prevention and treatment, which may help to reduce pollution from the source.

Sphalerite and copper sulfides often coexist in deposits, and cupric ions commonly used as additives to change the surface properties of sphalerite during flotation or hydrometallurgy processes (Bagheri et al., 2020; Zhang et al., 2020a). Therefore, cupric ions and sphalerite inevitably exist simultaneously in tailings and thus in AMD environments. Although copper and zinc both are the indispensable elements for life, excessive emission is potentially toxic (Xie et al., 2019; Yang et al., 2020). Therefore, investigating the action mechanism of copper ions on the dissolution of sphalerite (marmatite) may be of great significance to the control of copper and zinc in AMD.

Sphalerite (ZnS) is one of the most important zinc containing mineral resource in the earth. During the mineralization process, impurities like

* Correspondence to: School of Minerals Processing & Bioengineering, Central South University, No. 932 Lushan South Road, Yuelu District, Changsha 410083, Hunan, China.
E-mail addresses: zhbalexander@csu.edu.cn, alexandercsu@126.com (H. Zhao).

https://doi.org/10.1016/j.jhazmat.2020.124058
Received 22 July 2020; Received in revised form 23 August 2020; Accepted 20 September 2020
Available online 22 September 2020

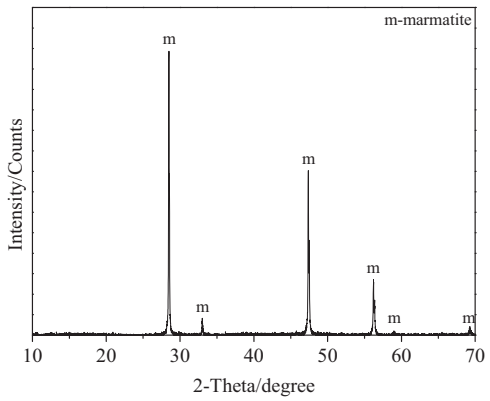

Fig. 1. XRD analysis of the purified marmatite sample (Zhang et al., 2020b).

iron (Fe) replaced zinc sites in the lattice structure of sphalerite and formed marmatite ($Zn_xFe_{1-x}S$. In this work, marmatite means sphalerite containing high percentages of iron.) with various high percentages of iron element and exhibited dark-black color (Cook et al., 2009; Liu et al., 2018). The structure (Chen et al., 2010b; Osadchii and Gorbaty, 2010), and dissolution behaviors (Weisener et al., 2004) also can be altered due to the iron incorporation. The crystal structure belongs to *F-3m* space group, and the (Zn, Fe) atom is located at (000) site and S atom at (0.250.250.25) site. The unit cell of marmatite is consisting of four Zn or Fe atoms and four sulfur atoms with cell parameters of $a = b = c = 0.54$ nm, $\alpha = \beta = \gamma = 90^\circ$, cell volume of 0.158 nm^3 (Edelbro et al., 2003; McIntyre et al., 1980). Except for iron element, some other minor and trace elements, such as Ag, Cd, Sn, Cu, In, Ge, Ga, Co, are also commonly incorporated in zinc sulfides (Cook et al., 2009).

Cupric ion (Cu^{2+}) as an important metal ion additive in the flotation processes of sphalerite (marmatite) was considered that the Cu^{2+} adsorption can form trace amount of copper sulfide on the surface and changed the surface properties, thus enhancing the surface reactivity with flotation collectors (Chandra and Gerson, 2009; Qiu et al., 2017). Similarly, Cu^{2+} has also been widely reported as catalyst in hydrometallurgy of zinc sulfides (Pathak et al., 2017), in which the formation of copper sulfides on marmatite surface was proposed but the detailed information and generation mechanism are still not clearly and completely interpreted (Meng et al., 2019; Zhang et al., 2020b).

In a previous work, Elliot and Watling (2011) found that pyrrhotite ($Fe_{1-x}S$) can be partly transformed to chalcopyrite ($CuFeS_2$) due to the incorporation of Cu^{2+} into pyrrhotite at normal pressure and temperature. Therefore, the present work utilized experimental techniques and theoretical calculations to explore the possibility of marmatite phase transformation in acidic solution (pH 0.5–4.5) in the presence of Cu^{2+}. Moreover, a strong correlation between the cupric ion consumption with the pH value variation was proposed and the effects of the added Cu^{2+} and the formed new phase on the dissolution kinetics of marmatite were discussed. The obtained results would not only help interpret the role of Cu^{2+} on sphalerite dissolution in AMD, but suggest the probable reason of the evolution of sphalerite and chalcopyrite symbiotic deposits.

2. Methodology

2.1. Transformation experiments

Marmatite samples were obtained from Guangxi Province of China. Result of X-ray diffraction (XRD) (Fig. 1 (Zhang et al., 2020b)) suggested that its purity was extremely high and almost no impurities coexisted. The chemical elements analysis of the sample showed it contained 48.28% Zn, 14.67% Fe, and 33.78% S respectively. Hence, it could be represented by the chemical formula $Zn_{0.74}Fe_{0.26}S$. Some highly purified samples were crushed and ground to less than 0.074 mm. In addition, some samples were cut into polished electrodes or tablets with diameter of about 10 mm and thickness of about 2 mm. In the transformation experiments, 0.25 g marmatite samples (or marmatite electrodes) were firstly added into each 250 mL flask containing different concentrations of aqueous copper solution (100 mL), which was adjusted by 10 g/L cupric ion solution (Prepared by Copper (II) sulfate pentahydrate, $CuSO_4{\cdot}5H_2O$, CAS number 7758-99-8, Analytical Reagent ($CuSO_4{\cdot}5H_2O \geq 99.0\%$), Batch No. 20150210, Sinopharm Chemical Reagent Co., Ltd, China). Flasks were placed in an orbital shaker with temperature of 75 °C (This temperature can be reached inside the mineral heap and in the mine waste recycling reactors.) and rotating speed of 170 rpm. In experimental systems of Section 3.2 (investigating the effects of pH values), pH values (Measured by Precision pH/ORP meter, BPP-920, Bell Analytical Instruments (Dalian) Co., Ltd.) were regularly controlled constantly by dilute sulfuric acid (Prepared by sulfuric acid, H_2SO_4, CAS number 7664-93-9, Analytical Reagent ($H_2SO_4 = 98.08\%$), Batch No. 20180821.1, Hunan Huihong Reagent Co., Ltd, China), while in experimental systems of Section 3.1 (investigating the effects of cupric ions concentrations) pH values were not adjusted. After reactions, solid and liquid samples were separated through washing and filtration.

2.2. Analytic techniques

Ion concentrations of copper, zinc and iron were regularly monitored by an inductively coupled plasma atomic emission spectrometry (ICP-AES) (ICAP 7400 Radial, Thermo Fisher Scientific Co.). Standard curves utilized in ICP-AES tests were established by using single element standard reference solutions of copper (Chinese national matter standard sample (GSB) 04-1725-2004, Unique Identification (UI) 192033-5), zinc (GSB 04-1761-2204, UI 17C035-1) and iron (GSB 04-1726-2004, UI 196002-7), they were all produced by National Nonferrous Metal and Electronic Materials Analysis and Testing Center, China. After treatment, solid samples were dried in vacuum oven (DZF, Huanghua Guangming Instrument Co.), and were then detected by different analytic techniques, including inVia Raman microscope combined with software Wise 5.0 (Renishaw Co.), synchrotron radiation-based X-ray diffraction (SR-XRD), X-ray micro-diffractometer (Rigaku D/max Rapid IIR), scanning electron microscopy (SEM) (JSM-6490LV/JEOL for treated samples and JSM-IT500LV/JEOL for treated samples), X-ray photoelectron spectroscopy (XPS) (ESCALAB 250Xi) and polarizing microscope (Leica-DM RXE). SR-XRD was conducted at beamline 4B9A in Beijing Synchrotron Radiation Facility (BSRF) in Beijing, China. X-ray diffraction (XRD) performed on X-ray micro-diffractometer with X-ray collimation of 0.1 mm in diameter was conducted at 40 kV and 250 mA (Cu Kα), with exposure time of 20 min and step length of 1°/s. Additionally, conventional X-ray diffraction (Bruker D8 Advance) was operated under the conditions of Cu Kα (2.2 kW), tube current of 40 mA, voltage of 40 kV, extra scanning range of 29–32° (2θ) and scanning speed of 0.5°/min. XPS analysis was recorded at a constant pass energy of 20 eV and 0.1 eV/step using an Al Kα X-ray source.

2.3. DFT calculations

Spin-polarized density functional theory (DFT) (Hohenberg and Kohn, 1964; Kohn and Sham, 1965) calculations were performed by using the plane-wave based Vienna ab-initio simulation package (VASP) (Kresse and Furthmüller, 1996). The generalized-gradient approximation (GGA) parametrized by Perdew–Burke–Ernzerhof (PBE) (Perdew et al., 1996) was used to treat the exchange-correlation functional. The interactions between atomic cores and electrons was represented through the projector augmented-wave (PAW) method of Blöchl (Blöchl, 1994; Kresse and Joubert, 1999) as implemented in VASP. An optimized cut-off energy of 400 eV was adopted throughout, which was found sufficient in optimization of slab models. In geometry optimizations, the total energy was converged to 10^{-5} eV, and forces acting on ions were required to be less than 0.01 eV/Å.

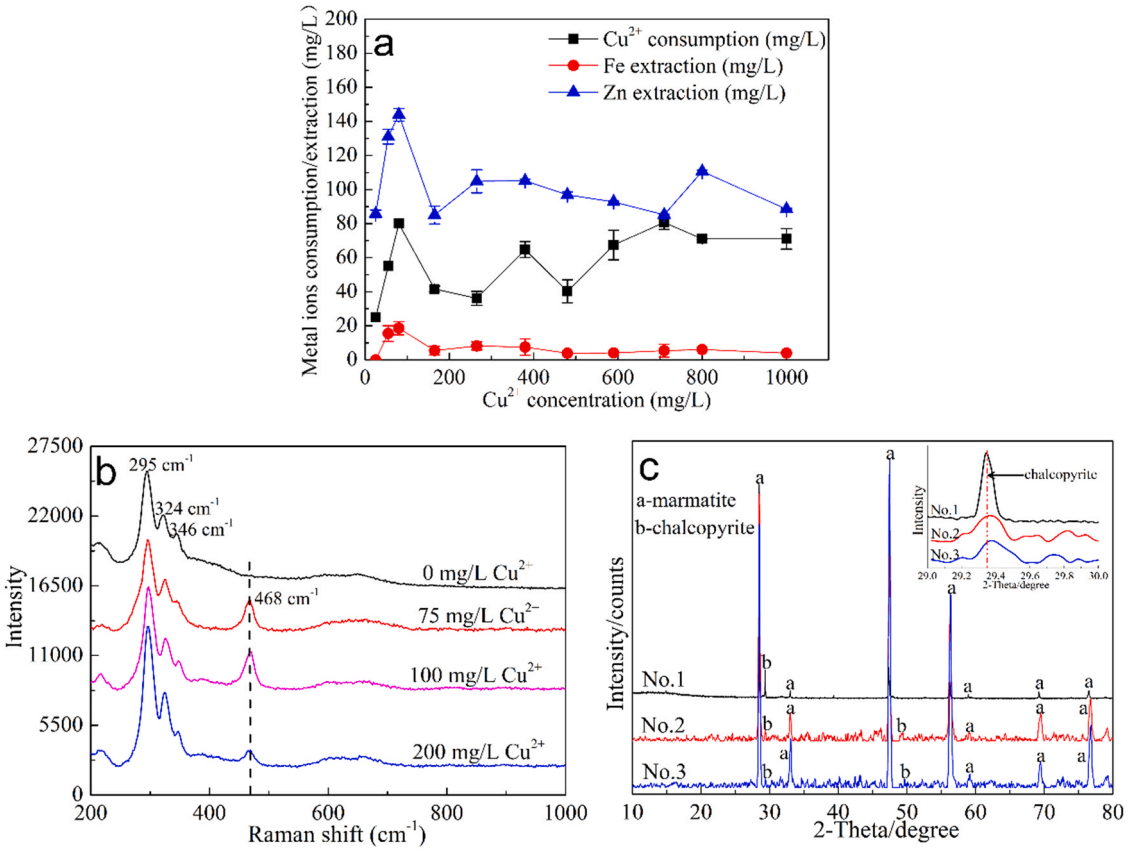

Fig. 2. Dissolution of marmatite in different cupric ion concentrations in 1 day (normal pressure, 75 °C, 170 rpm, cupric sulfate solution with pH uncontrolled): (a) metal ions consumption/extraction (The initial cupric ion concentrations shown on the abscissa axis were derived from the actual measurement); (b) Raman spectra of marmatite samples after treatment; (c) XRD of marmatite samples after treating by 100 mg/L Cu^{2+}: No. 1 (synchrotron radiation-based X-ray diffraction), No. 2 and 3 (X-ray micro-diffractometer, different locations).

To simulate sphalerite (110) surface, we used a model containing a 2 × 2 (110) slab with eight atomic layers, within which five Zn atoms were randomly replaced by Fe atoms with an approximate chemical formula of $Zn_{0.32}Fe_{0.18}S_{0.5}$. A vacuum layer of 15 Å was employed in the perpendicular direction to avoid spurious interactions between two images. In the calculations of the substitution and diffusion, all the atomic layers in the slab models were allowed to fully relax by using a conjugate-gradient algorithm. The Brillouin zone integrations were performed using Monkhorst–Pack scheme (Monkhorst and Pack, 1976) with a 3 × 4 × 1 *k*-point grids with a generalized Gaussian smearing method with the smearing width set to 0.05 eV.

The substitution energy of a Cu^{2+} ion for Zn^{2+} or Fe^{2+} ions of sphalerite (110) surface is calculated as:

$$E_{\text{sub}} = E^{sub}_{after} + \mu_{Zn^{2+}/Fe^{2+}} + E^{sub}_{before} - \mu_{Cu^{2+}} \quad (1)$$

where E^{sub}_{after} (eV) and E^{sub}_{before} (eV) are the total energies of the slab model after and before the substitution happens, whereas, μ (eV) is the chemical potential of these ions in the substitution in their isolated states. More negativity of E_{sub} (eV) is for a much easier substitution reaction to occur.

On the other hand, the diffusion energy (E_{dif} (eV)) of a Cu^{2+} ion on the surface into the body of sphalerite via site exchanging with nearby Zn^{2+} or Fe^{2+} ion is defined as:

$$E_{\text{dif}} = E^{dif}_{after} - E^{dif}_{before} \quad (2)$$

where $E^{\text{dif}}_{\text{after}}$ (eV) and E^{dif}_{before} (eV) are the total energies of the slab model after and before the diffusion happens.

3. Results

3.1. Effects of cupric ions concentrations

Firstly, the effects of cupric ions concentrations on the dissolution of marmatite were investigated. Marmatite samples were soaked in the different cupric ion solutions with concentrations from 50 to 1000 mg/L, and the pH values were uncontrolled. After 1 day, the results indicated that a fraction of cupric ions was consumed, along with the decomposition of marmatite (Fig. 2a). The appearance of samples treated by different cupric ion concentrations was also changed, as shown in Supplementary materials Fig. 1s. Typically, the group with around 100 mg/L initial cupric ions showed the most obvious distinctions, exhibiting the high extractions of iron and zinc as well as the high consumption of cupric ions. Furtherly, Raman spectroscopy, SR-XRD, X-ray micro-diffractometer (micro-XRD) and X-ray diffractometer (XRD) were utilized to characterize the treated samples (Fig. 2b, c and Supplementary materials Fig. 2s). Compared with the group without cupric ions, an extra new Raman peak appeared at the position of 468 cm^{-1} in the groups with cupric ions, which represented the existence of Cu–S bonds (White, 2009; Żmuda-Trzebiatowska et al., 2016). Although the existence of Cu–S bond was confirmed, the exact Cu mineral phase was still uncertain as the Cu–S bond could belong to several copper sulfides such as chalcopyrite and covellite (Żmuda-Trzebiatowska et al., 2016). Therefore, XRD (SR-XRD, micro-XRD and general XRD of marmatite samples after treating by 100 mg/L Cu^{2+}) was performed in order to furtherly detect the Cu mineral phase. As shown in Fig. 2c, the new peaks marked as *b* were located at around 29 and 59°, which might be attributed to the (112) crystal plane and the (204) crystal plane of chalcopyrite, respectively (Majuste et al., 2013). As the chalcopyrite

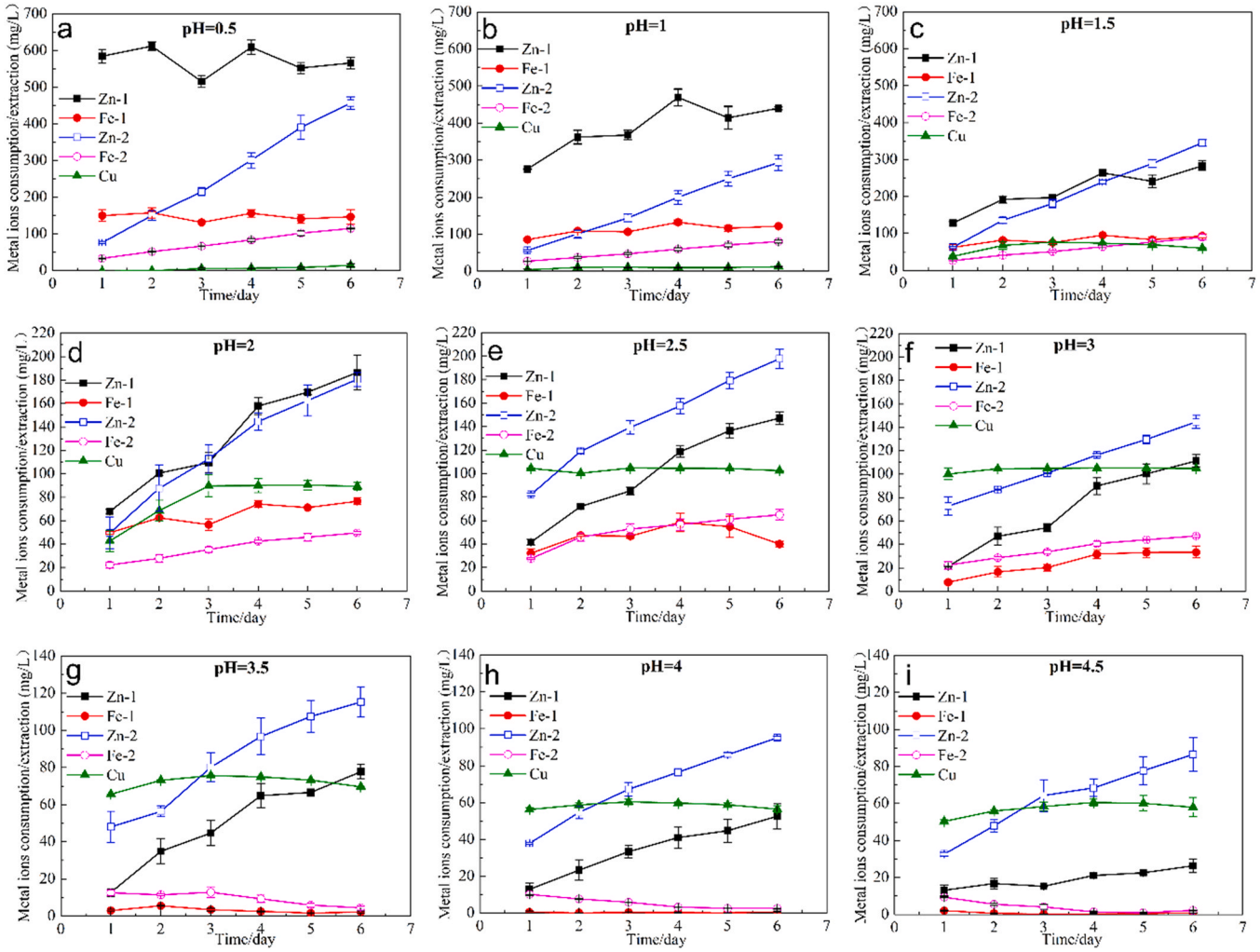

Fig. 3. Dissolution of marmatite in different pH conditions (normal pressure, 75 °C, 170 rpm, in the presence and absence of 100 mg/L Cu^{2+}): (a–i) pH values are 0.5, 1.0, 1.5, 2.0, 2.5, 3.0, 3.5, 4.0 and 4.5, respectively. Zn-1 and Fe-1 represent zinc and iron extraction in the absence of Cu^{2+}; Zn-2 and Fe-2 represent zinc and iron extraction in the presence of 100 mg/L Cu^{2+}; Cu was Cu^{2+} consumption.

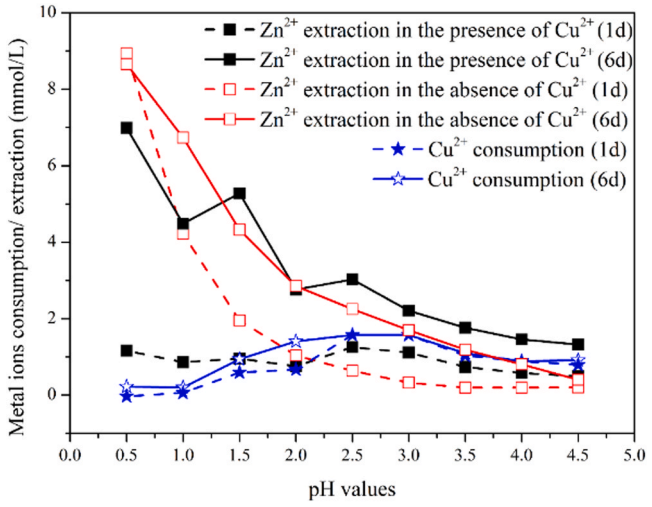

Fig. 4. Dissolution of marmatite in different pH conditions in the first day and the last day (normal pressure, 75 °C, 170 rpm, in the presence and absence of 100 mg/L Cu^{2+}).

phase was not originally present in the samples, it suggested that the consumed cupric ions might occupied segmental lattice sites of marmatite which originally belong to zinc and iron, causing the formation of chalcopyrite phase.

3.2. *Effects of pH values*

Subsequently, a series of experiences with pH value variables were performed for the most effective cupric ion concentration of 100 mg/L. Fig. 3 demonstrates the zinc and iron extractions in the presence and absence of cupric ions, and the cupric ion consumptions. In general, with the increase of pH values, the dissolution rate of marmatite samples decreased gradually both with and without the addition of cupric ions, which was coincide with the previous reports (Acero et al., 2007; Stanton et al., 2008). Additionally, the presence of cupric ions apparently impeded the dissolution of marmatite at pH = 0.5 and 1.0 (Fig. 3a and b), and slightly affected marmatite dissolution at pH = 1.5 and 2.0 (Fig. 3c and d), but obviously enhanced marmatite dissolution at pH = 2.5–4.5 (Fig. 3e–i). This phenomenon suggests that the effect of cupric ions on marmatite dissolution is related to the pH values. Fig. 3 shows that the consumptions of cupric ions are tend to stable only after 1 day, the dissolution behavior of marmatite after the first day is therefore analyzed as shown in Fig. 4. On the other hand, the dissolution of marmatite is a continuous process, so data of the last day is also

Table 1
Several E_a values summarized by Acero et al. (2007).

pH values	< 0.5	< 1	1	2	2	3
Fe (wt%)	0.3–2.15	0.1–0.45	0.5	6.2	1.0	0.1
E_a (kJ/mol)	83.4	37.4–44.3	34 ± 4	46.9 ± 11.3	27	14.3 ± 1.9

showed in Fig. 4.

According to Fig. 4, in the absence of Cu^{2+}, the dissolution rate of marmatite changes obviously with the increase of pH values. Acero et al. (2007) summarized different reports about the apparent activation energies (E_a, as shown is Table 1) of sphalerite dissolution in various pH values with the temperature around 20–90 °C. They suggested that $E_a < 20$ kJ/mol usually meant transport-controlled mechanisms (diffusional control). Moreover, according to the kinetic regimes research of Lorenzo-Tallafigo et al. (2018), $E_a > 40$ kJ/mol normally indicated sphalerite dissolution was under chemical control. Combined with the dissolution curve of marmatite in the absence of Cu^{2+} in Fig. 4, it may speculate that when the pH value is less than 1, between 1.5 and 2.5, and greater than 3, marmatite dissolution are respectively in chemical control, mixed control and diffusional control.

Besides, Fig. 4 shows that when the pH value is less than 2, the addition of Cu^{2+} impedes the dissolution of marmatite both after the first and the last day, but when the pH value is greater than 2, the situation is reversed. Especially, marmatite dissolution was obviously inhibited in the first day by adding Cu^{2+}. According to the Raman and XRD results (Fig. 2b and c), a Cu-bearing thin layer might be formed on marmatite surface. It indicated that this thin layer may slow down the chemical reaction rate of marmatite when the pH value is less than 2, and the kinetic regimes may be shifted from chemical control (in the absence of Cu^{2+} with the same pH range) to mixed control or diffusional control. However, although the formed Cu-bearing thin layer slow down the chemical reaction rate under chemical control, it may promote the surficial electrochemical property of marmatite, thus accelerating its dissolution under mixed control or diffusional control stages. The phenomenon that the high Zn^{2+} extraction in the presence of Cu^{2+} after 6d is therefore explained. Moreover, Fig. 4 shows that when the pH value is greater than 2 (under mixed control or diffusional control), the dissolution of marmatite is accelerated both after the first and the last day in the presence of Cu^{2+}, which may furtherly prove this inference.

Then the consumption of Cu^{2+} was analyzed, which was increased at first from pH = 0.5 to pH = 2.5, while declined from pH = 3.0 to pH = 4.5. Especially, at pH = 0.5 and 1.0, only a slight of cupric ions were consumed. Fig. 3e and f show that the cupric ions are consumed totally at pH = 2.5 and 3.0, even requiring only 1 day. According to these results, there is a possible mechanism. The consumption of cupric ions depends on the amount of the lattice vacancies in marmatite matrix. In more detail, four transformation states can be defined according to changes in pH values. The first state, at pH = 0.5 and 1.0 (Fig. 3a and b), only a slight of cupric ions were consumed and the marmatite was dissolved sufficiently after 6 days. On the one hand, the formed Cu-bearing species might be unstable in the low pH environment. On the other hand, the interface lattices of marmatite were broken entirely, so lattice vacancies were more difficult to available. Therefore, almost no cupric ions are consumed. The second state, pH = 1.5 and 2.0, the dissolution rate of marmatite is gradually slowed down (Fig. 3c and d), and more and more destroyed lattices with vacancies occurred. As the number of

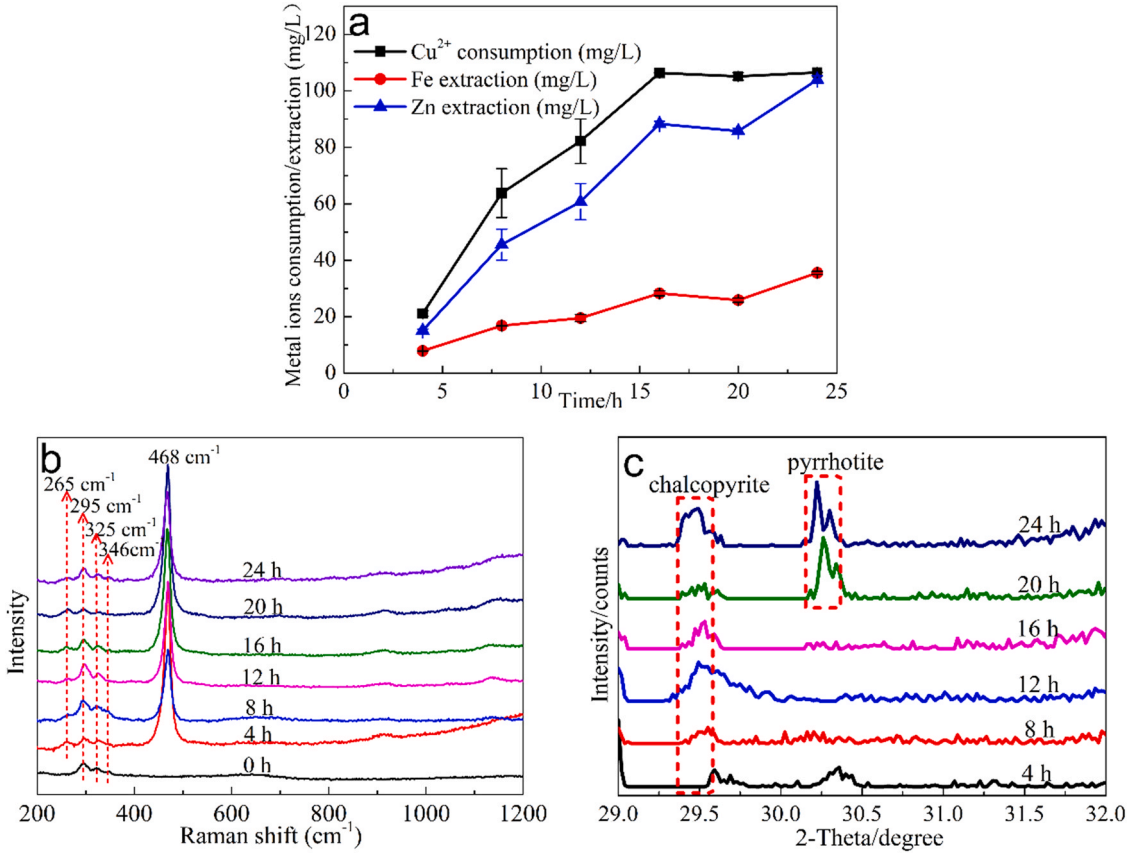

Fig. 5. (a) Dissolution of marmatite at pH = 2.5 (normal pressure, 75 °C, 170 rpm, in the presence of 100 mg/L Cu^{2+}); (b) Raman spectra and (c) XRD of marmatite samples after different hours of treatment.

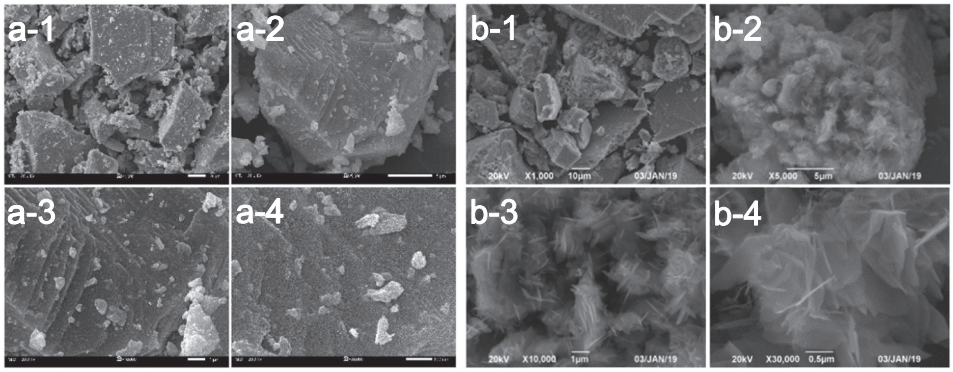

Fig. 6. SEM images of marmatite samples before (a) and after (b) treated with 100 mg/L Cu^{2+} at pH = 2.5, normal pressure, 75 °C, 170 rpm for 24 h: (a-1, b-1) ×1000; (a-2, b-2) ×5000; (a-3, b-3) ×10,000; (a-4, b-4) ×30,000.

vacancies increased, the consumption of cupric ions followed by. Until the third state, pH = 2.5 and 3.0, all cupric ions entered the lattices (Fig. 3e and f). Finally, the fourth state, when the pH is excessive high (pH > 3.0), zinc and iron extractions are declined gradually (Fig. 3g–i), producing fewer lattice vacancies and thus consuming lesser cupric ions. Fig. 4 also shows that when the pH value is greater than 2, the trend of Cu^{2+} consumption coincides with that of Zn^{2+} extraction. Considering that sphalerite and chalcopyrite having similar crystal structures (Cama et al., 2006; Li et al., 2013), it is likely that chalcopyrite is formed after the substitution of zinc by copper.

The iron extraction trend at pH < 3.5 was similar as that of zinc, but when pH > 3.5, extractions of iron were very low, especially in the absence of cupric ions, which might be due to the formation of $Fe(OH)_3$ precipitation. In fact, at higher pH conditions, the amount of dissolved oxygen may increase relatively, thereby accelerating the oxidation rate of ferrous to ferric (Qian et al., 2018; Zhou et al., 2018). Therefore, most of the iron ions were subsequently precipitated (Fig. 2g–i).

3.3. Analysis of surface species

According to the results of Sections 3.1 and 3.2, the most distinct experiment settings of 100 mg/L cupric ions cooperating with the pH of 2.5 were confirmed. Additionally, since almost no cupric ions were consumed after the first day, sampling at shorter intervals in 1 day was implemented. In these cases, the zinc and iron extractions and cupric ions consumption results are shown in Fig. 5a. Before 15 h, as time went on, both the metal ions consumption and extractions were increasing. Around 15 h later, the added cupric ions were consumed entirely.

Fig. 5b and c shows the Raman spectra and XRD of marmatite samples after different hours of treatment. In addition to the apparent Raman peak at 468 cm^{-1}, another extra peak at 265 cm^{-1} was observed. This extra peak might be related to the partial Cu–S bonds of chalcopyrite (White, 2009). Moreover, the Raman peaks at 346 cm^{-1} representing the Zn–S bonds of marmatite (Buzatu et al., 2013) were quite weak in several groups (12 h, 16 h and 20 h). Therefore, it is suspected that with the release of zinc from the marmatite lattices, copper ions enter and occupy the vacancies. Hence, Cu–S bonds appear, and it is highly probable that the chalcopyrite structure is formed partially.

The results of XRD furtherly illustrated two new peaks at around 29.5 and 32.5°, which might belong to chalcopyrite and pyrrhotite, respectively (Majuste et al., 2013; Mikhlin et al., 2002). In addition to the detected chalcopyrite peaks, Elliot and Watling (2011) proposed that pyrrhotite could be converted to chalcopyrite under acidic conditions with the existence of cupric ions. Combined with the theory of Elliot and Watling, a supplement at the front end probably can be made, that is the conversion from marmatite to pyrrhotite (Eqs. (3, 4)) (Lan et al., 2009). Additionally, another study (Keith et al., 2014) proposed that the formation of chalcopyrite and pyrrhotite inclusions in bulk sphalerite were common in high temperature environments (around 300 °C), which provided support for the possibility of chalcopyrite and pyrrhotite formation in this work to some extent.

$$Zn_{(1-x)}Fe_xS + 0.5O_2 + 2H^+ \rightarrow (1-x)Zn^{2+} + yFe^{2+} + (x-y)FeS + (1-x+y)S^0 + H_2O \quad (3)$$

$$FeS + 2xH^+ + 0.5xO_2 \rightarrow Fe_{1-x}S + xFe^{2+} + xH_2O \quad (4)$$

Fig. 6 shows the SEM images of some regional locations of the marmatite before and after treated with four different resolutions. Compared with the images of the initial sample, the morphology of marmatite surface was coarse after treated at pH = 2.5 for 24 h. The formed crystalline substances were clearly not part of the initial

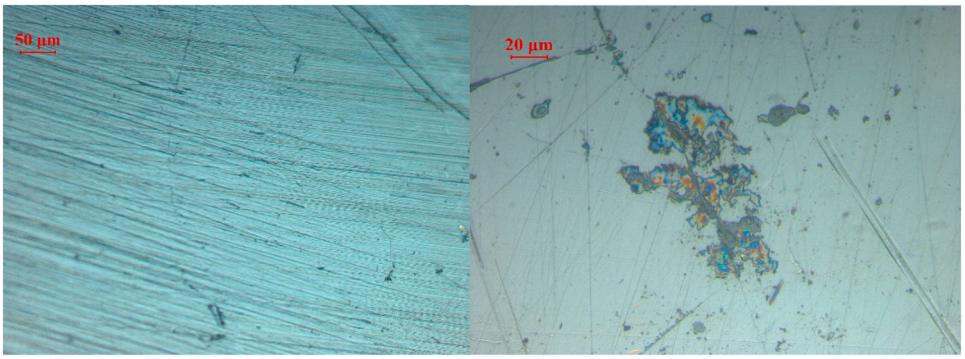

Fig. 7. Polarizing microscope images of marmatite samples with (left) and without (right) treatment at pH = 2.5 for 24 h (normal pressure, 75 °C, 100 mg/L Cu^{2+}, 170 rpm).

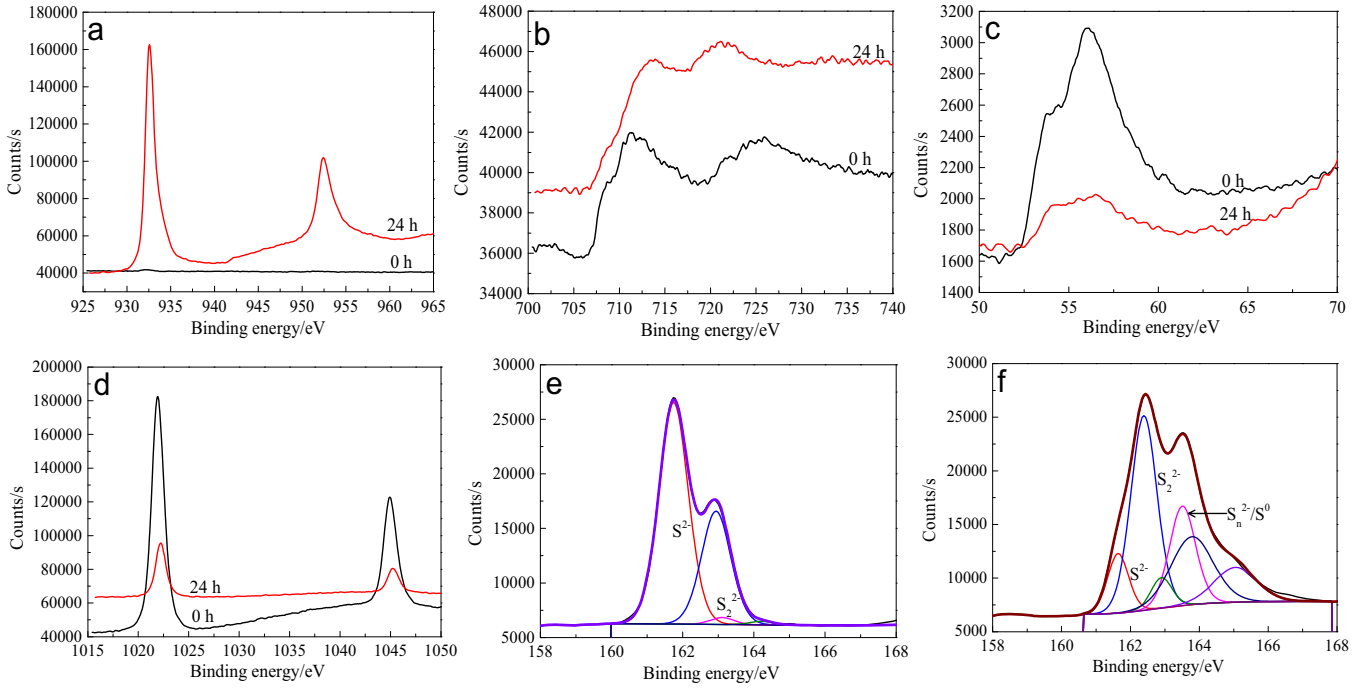

Fig. 8. XPS spectra of Cu 2p (a), Fe 2p (b), Fe 3p (c), Zn 2p (d) and S 2p (e – initial marmatite and f – treated marmatite) of marmatite with and without treatment at pH = 2.5 for 24 h (normal pressure, 75 °C, 100 mg/L Cu^{2+}, 170 rpm).

marmatite. Subsequently, SEM–EDS analysis was performed for these substance and results proved that 12.62 wt% copper was contained in the formed new phase (Supplementary materials Fig. 3s). Fig. 7 shows the polarizing microscope images of the untreated and treated marmatite tablets. After treatment, the morphology of the fracture zone of marmatite surface changed significantly. Therefore, it was likely that new copper-bearing phases were formed after treatment.

Furtherly, the surface species was analyzed using XPS. Fig. 8 shows the XPS spectra of Cu 2p, Fe 2p, Fe 3p, Zn 2p and S 2p of marmatite before and after treatment. As shown in Fig. 8a, two typical Cu 2p peaks (Cu $2p_{3/2}$ peak at around 932 eV and Cu $2p_{1/2}$ peak at around 952 eV) occurred after the treatment of cupric ions, which might be related to the binding energy of Cu species, such as chalcopyrite, bornite, chalcocite and covellite (Matsuoka et al., 2020; Mezgebe et al., 2019). Then, Fe 2p, Fe 3p and Zn 2p spectra are shown in Fig. 8b–d in sequence. Apparently, the characteristic peak areas of them all decreased after the treatment of Cu^{2+} for 24 h, which reflected the extraction results of the above.

However, S 2p spectra shown in Fig. 8e and f demonstrate that the S atom proportion of marmatite surface is augmented after treatment. By using the software Thermo Avantage 5.52, these XPS spectra were further fitted. In this process, charge correction was accomplished by referring to the C 1s level at 284.8 eV, the background was obtained using the Shirley method, and the peaks fitted to the corresponding spectra were achieved using the Gaussian–Lorentzian line (SGL) function (Shirley, 1972). Results suggested that monosulfide (S^{2-}) was the main chemical state of S before treatment (Fig. 8e), while disulfide (S_2^{2-}) and polysulfide (S_n^{2-}/S^0, $n > 2$) formed after treatment (Fig. 8f). Equations (5–8) described the possible formation process of them (Weisener et al., 2004). And the insoluble and non-conductive polysulfide may passivate the marmatite surface in acidic positions (pH < 6.0) (Heidel et al., 2011), and should be the reason of rate-limiting of mixed control and diffusional control (Cama et al., 2006).

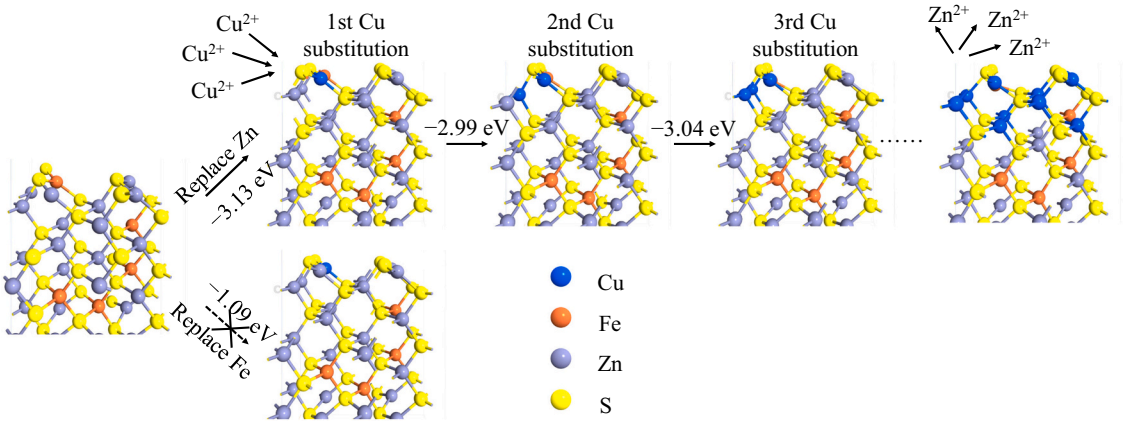

Fig. 9. Illustration of the ion exchange mechanism in the sphalerite at low concentrations of Cu^{2+}. Route 1 represents for the Zn sites on the (110) surface of sphalerite replaced by the 1st, 2nd, and 3rd Cu ions with the substitution energies of approximately − 3 eV, meanwhile it results in 1:1 release of Zn ions into the solution. Route 2 denote the Fe sites on the (110) surface of sphalerite replaced by the Cu ions, however, it is less energetically favorable than route 1 since the substitution energy of ~− 1 eV is much more positive than that of route 1.

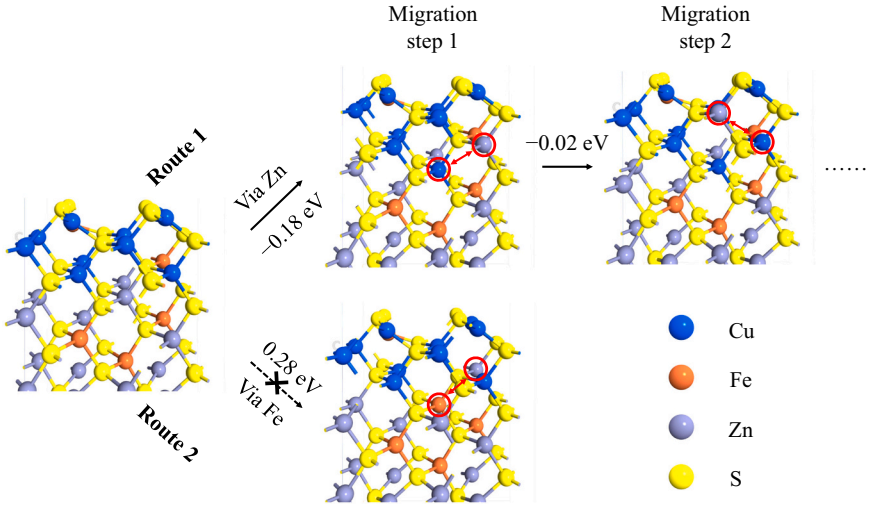

Fig. 10. Illustration of the site exchange mechanism in the sphalerite at high concentrations of Cu^{2+}. Route 1 represents for the migration of surface Cu via site exchanging with nearby Zn and finally diffuse into the body of sphalerite is a facile process with small energy changes for different migration steps of − 0.18 and − 0.02, respectively. Route 2 denote the migration of surface Cu via site exchanging with nearby Fe, however, it is less energetically favorable than route 1 since the energy change of ~0.28 eV for the migration step 1 is much more positive than that of route 1.

$$2S^{2-}_{(s)} + 2H^+ + 0.5O_2 \rightarrow S^{2-}_{2\ (s)} + H_2O \quad (5)$$

$$3S^{2-}_{(s)} + 4H^+ + O_2 \rightarrow S^{2-}_{3(s)} + 2H_2O \quad (6)$$

$$8S^{2-}_{(s)} + 12H^+ + 3O_2 \rightarrow 2S^{2-}_{4(s)} + 6H_2O \quad (7)$$

$$2S^{2-}_{(s)} + 4H^+ + O_2 \rightarrow 2S^{0}_{(s)} + 2H_2O \quad (8)$$

3.4. DFT calculations

To validate the experimental observations at the atomic scale, DFT calculation were further calculated to study the reaction mechanism of the Cu^{2+} substitution and migration in the marmatite. According to previous study (Chen et al., 2010a), the first layer of Zn sites for Cu substitution is more energetically favorable, therefore we only consider the seven Zn sites and one Fe site for the Cu substitution on the surface of modeled sphalerite (110). Based on the calculation results, the calculated E_{sub} is − 3.13 eV when one of the Zn sites is replaced by the first Cu, compared to that of − 1.09 eV for Fe site, which indicates that Cu ions would incorporate into Zn site when they are approaching to the surface of sphalerite with release of Zn ions into solution. Considering that the substitution energy is significantly negative for this process, this ion exchange mechanism will continue to take place with the second and third Cu substitution (− 2.99 and − 3.04 eV respectively), and finally results in 1:1 release of Zn ions approximately when increases the concentration of Cu ions, as shown in Fig. 9.

At higher concentration of Cu ions, as pointed out by Gerson et al. (1999), further substitutions to the subsequent layers of sphalerite would occur by the site exchange mechanism where the Cu in the first layer will diffuse into the Zn site in the second layer or by interstitial movement of Cu atom. To confirm this possible mechanism, we also carried out DFT calculations to study the diffusion path of Cu migration when upper several layers are uptake by Cu ions. As shown in Fig. 10, route 1 represents for the migration of surface Cu via site exchanging with nearby Zn and finally diffuse into the body of sphalerite. The calculated E_{dif} for different migration steps are − 0.18 and − 0.02 eV respectively, which indicates that it is a facile process with small energy changes. In comparison, route 2 denotes the migration of surface Cu via site exchanging with nearby Fe, however, it is less energetically favorable than route 1, since the energy change of ~0.28 eV for the migration step 1 is much more positive than that of route 1.

4. Discussion

Results of the batch experiments (Effects of cupric ions concentrations and pH values) showed that the highest Zn^{2+} extraction is acquired with Cu^{2+} concentration around 100 mg/L in the condition of pH uncontrolled (Fig. 2a). Additionally, the added 100 mg/L Cu^{2+} was consumed quickly and entirely at pH 2.5 and 3.0 (Fig. 3). Results of SEM–EDS (Supplementary materials Fig. 3s) and XPS spectra of Cu 2p (Fig. 8a) revealed that the consumed Cu^{2+} was transferred to the surface of marmatite. Similarly, Liao et al. (2019) reported that a Cu-containing layer with several nanometers on sphalerite surface was formed after being soaked in a Cu^{2+} solution without any other processes, while the further information about the new phase, the extraction of Zn^{2+} and the effects of pH values was absent. Subsequently, results of Raman spectra (Figs. 2b and 5b) confirmed that the new Cu–S bond (265 cm^{-1} and 468 cm^{-1}) occurred on marmatite surface after treated but the exact Cu phase was still uncertain (White, 2009; Żmuda-Trzebiatowska et al., 2016). According to the research of (Meng et al., 2019), a passivation surface layer containing Cu–S and Cu–O species was formed during marmatite dissolution with high Cu^{2+} concentration in the solution. And in our another work (Zhang et al., 2020b), the interaction mechanism between marmatite and chalcocite in acidic (microbial) environments was discussed, from which the speculation of the new mineral phase on marmatite surface was proposed. In this work, three kinds of XRD were therefore carried out for the treated samples to study the new phase, and results suggested that three new XRD peaks occurred, in which peaks located around 29.5 and 59° could be attributed to chalcopyrite (Majuste et al., 2013), and peaks located around 32.5° could result from the formation of pyrrhotite (Mikhlin et al., 2002). In addition to the formation of chalcopyrite peaks, the occurrence of pyrrhotite might also provide a considerable mineral phase conversion pathway from marmatite to pyrrhotite ($Fe_{1-x}S$) (Eqs. (3, 4) (Lan et al., 2009)), then from pyrrhotite ($Fe_{1-x}S$) to copper-pyrrhotite ($CuFe_7S_8$) to unnamed mineral $CuFe_3S_4$ to isocubanite ($CuFe_2S_3$) and finally to chalcopyrite ($CuFeS_2$) (Elliot and Watling, 2011).

In order to explore the possibility and mechanism of Cu^{2+} entering the marmatite lattices, DFT calculation were further calculated. Results suggested that Cu^{2+} would easily incorporate into Zn site on marmatite surface with the E_{sub} around −3 eV (Fig. 9), and migration into the deeper layer also was proved to be possible (E_{dif} are −0.18 and −0.02 eV) (Fig. 10). However, the substitution (−1.09 eV) and migration (0.28 eV) at Fe site were difficult. The selective substitution of copper for zinc in marmatite lattice provided important conditions for the production of chalcopyrite.

Subsequently, the effects of the added Cu^{2+} and the formed new

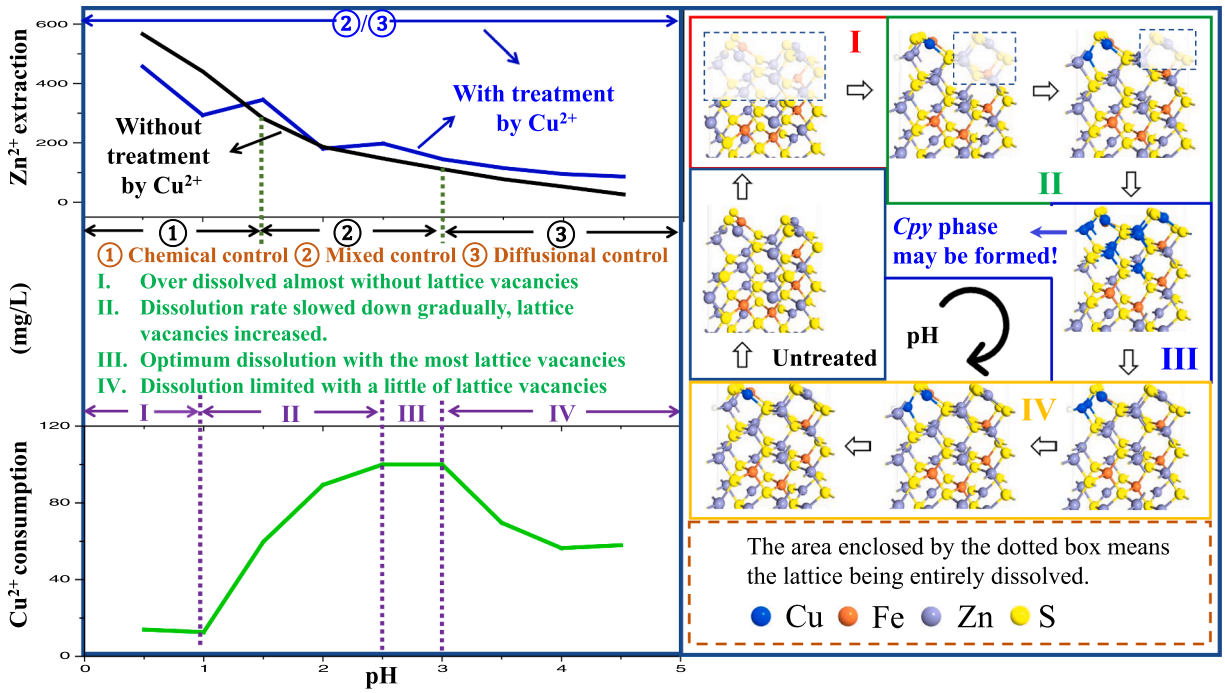

Fig. 11. Schematic of the interface phase transformation of marmatite matrix in aqueous copper solution at normal pressure and temperature and the mechanism of Cu^{2+} consumption with a change in pH: Data of Cu^{2+} consumption and Zn^{2+} extraction after 6 days were shown. Marmatite dissolution without Cu^{2+} could be divided into three stages according to pH values: chemical control, mixed control and diffusional control, while, only mixed control and diffusional control were existed in the presence of Cu^{2+}. The consumption of Cu^{2+} might depend on the amount of the lattice vacancies in marmatite matrix, including four transformation states defined according to changes in pH values. The most distinct settings of 100 mg/L Cu^{2+} cooperating with the pH of 2.5 was confirmed, in which all the added Cu^{2+} was consumed and the new chalcopyrite phase might be formed.

phase on the dissolution kinetics of marmatite were researched. Results of Figs. 3 and 4 indicate that marmatite dissolution can be promoted with 100 mg/L Cu^{2+} when the pH values > 2, and impeded when the pH values < 2. According to the E_a researches shown in Acero et al. (2007) and Lorenzo-Tallafigo et al. (2018), three kinetic regimes (without Cu^{2+}) were proposed that respectively are chemical control (pH < 1), mixed control (1.5 < pH < 2.5) and diffusional control (pH > 3). The formed new phase may shift the kinetic regimes from chemical control to mixed control or diffusional control in the low pH range (pH < 2), thus inhibiting marmatite dissolution. But it could promote the surficial electrochemical property of marmatite which may accelerate the dissolution rate of marmatite in mixed control or diffusional control stages. Furtherly, a model of the Cu^{2+} consumption mechanism during marmatite dissolution with a change in pH was proposed as discussed in Section 3.2. Finally, a schematic diagram of this work is shown in Fig. 11.

5. Conclusions

At normal pressure and temperature, marmatite dissolution was affected by the added Cu^{2+} and changes in pH values (0.5–4.5). At the most distinct settings of 100 mg/L Cu^{2+} cooperating with pH 2.5, all Cu^{2+} was consumed and the new chalcopyrite phase was very likely formed. The phase transition path might be from marmatite (to pyrrhotite) to chalcopyrite by the selective substitution and migration of Cu^{2+} on Zn sites of marmatite lattice. Furtherly, the occurred new phase could impede marmatite dissolution by shifting the kinetic regimes from chemical control to mixed control or diffusional control compared to the Cu^{2+}-free conditions at pH < 1.5, while accelerate marmatite dissolution at pH > 1.5 by promoting the surficial electrochemical property under mixed control or diffusional control stages. About the relation between Cu^{2+} consumption and pH value variation, a mode was proposed that the substitution of Cu^{2+} depends on the amount of the lattice vacancies in sphalerite matrix: most of the interface lattices are entirely destroyed in the over dissolved range (pH < 1.0) of marmatite, and few metal ions are released in the slow dissolving ranges (1.0 < pH < 2.5, pH > 3.0), therefore, fewer lattice vacancies result in the low cupric ion substitutions; but for the optimum dissolution range (2.5 < pH < 3.0), the largest cupric ion substitution should attribute to the adequate lattice vacancies.

CRediT authorship contribution statement

Yisheng Zhang: Investigation, Data curation, Writing - original draft. **Hongbo Zhao:** Resources, Funding acquisition, Project administration, Writing - review & editing, Validation. **Xiaoyu Meng:** Investigation. **Pengfei Ou:** Investigation. **Xin Lv:** Investigation. **Luyuan Zhang:** Writing - review & editing. **Lixin Liu:** Writing - review & editing. **Fashang Chen:** Writing - review & editing. **Guanzhou Qiu:** Funding acquisition.

Declaration of Competing Interest

The authors declare that they have no known competing financial interests or personal relationships that could have appeared to influence the work reported in this paper.

Acknowledgements

This work was supported by the National Natural Science Foundation of China (51704331), Open Foundation of State Key Laboratory of Mineral Processing, China (BGRIMM-KJSKL-2020-06) and the Open Funds of Beijing Synchrotron Radiation Facility, China (2017-BEPC-PT-000466).

Appendix A. Supporting information

Supplementary data associated with this article can be found in the online version at doi:10.1016/j.jhazmat.2020.124058.

References

Acero, P., Cama, J., Ayora, C., 2007. Sphalerite dissolution kinetics in acidic environment. Appl. Geochem. 22, 1872–1883.

Akcil, A., Koldas, S., 2006. Acid mine drainage (AMD): causes, treatment and case studies. J. Clean. Prod. 14, 1139–1145.

Bagheri, B., Vazifeh Mehrabani, J., Farrokhpay, S., 2020. Recovery of sphalerite from a high zinc grade tailing. J. Hazard. Mater. 381, 120946.

Blöchl, P.E., 1994. Projector augmented-wave method. Phys. Rev. B 50, 17953–17979.

Buzatu, A., Buzgar, N., Damian, G., Vasilache, V., Apopei, A.I., 2013. The determination of the Fe content in natural sphalerites by means of Raman spectroscopy. Vib. Spectrosc. 68, 220–224.

Cama, J., Acero, P., Ayora, C., 2006. Comparison between chalcopyrite and sphalerite dissolution kinetics under ARD conditions. Geochim. Cosmochim. Acta. 70, A80.

Chandra, A.P., Gerson, A.R., 2009. A review of the fundamental studies of the copper activation mechanisms for selective flotation of the sulfide minerals, sphalerite and pyrite. Adv. Colloid Interface 145, 97–110.

Chen, J.H., Chen, Y., Li, Y.Q., 2010. Quantum-mechanical study of effect of lattice defects on surface properties and copper activation of sphalerite surface. Trans. Nonferrous Met. Soc. 20, 1121–1130.

Chen, Y., Chen, J., Guo, J., 2010. A DFT study on the effect of lattice impurities on the electronic structures and floatability of sphalerite. Miner. Eng. 23, 1120–1130.

Cook, N.J., Ciobanu, C.L., Pring, A., Skinner, W., Shimizu, M., Danyushevsky, L., Saini-Eidukat, B., Melcher, F., 2009. Trace and minor elements in sphalerite: a LA-ICPMS study. Geochim. Cosmochim. Acta 73, 4761–4791.

Edelbro, R., Sandström, Å., Paul, J., 2003. Full potential calculations on the electron bandstructures of sphalerite, pyrite and chalcopyrite. Appl. Surf. Sci. 206, 300–313.

Elliot, A.D., Watling, H.R., 2011. Chalcopyrite formation through the metathesis of pyrrhotite with aqueous copper. Geochim. Cosmochim. Acta 75, 2103–2118.

Gerson, A.R., Lange, A.G., Prince, K.E., Smart, R.S.C., 1999. The mechanism of copper activation of sphalerite. Appl. Surf. Sci. 137, 207–223.

Heidel, C., Tichomirowa, M., Breitkopf, C., 2011. Sphalerite oxidation pathways detected by oxygen and sulfur isotope studies. Appl. Geochem. 26, 2247–2259.

Hohenberg, P., Kohn, W., 1964. Inhomogeneous electron gas. Phys. Rev. 136, B864–B871.

Jin, D., Wang, X., Liu, L., Liang, J., Zhou, L., 2020. A novel approach for treating acid mine drainage through forming schwertmannite driven by a mixed culture of *Acidiphilium multivorum* and *Acidithiobacillus ferrooxidans* prior to lime neutralization. J. Hazard. Mater. 400, 123108.

Keith, M., Haase, K.M., Schwarz-Schampera, U., Klemd, R., Petersen, S., Bach, W., 2014. Effects of temperature, sulfur, and oxygen fugacity on the composition of sphalerite from submarine hydrothermal vents. Geology 42, 699–702.

Kohn, W., Sham, L.J., 1965. Self-consistent equations including exchange and correlation effects. Phys. Rev. 140, A1133–A1138.

Kresse, G., Furthmüller, J., 1996. Efficient iterative schemes for ab initio total-energy calculations using a plane-wave basis set. Phys. Rev. B 54, 11169–11186.

Kresse, G., Joubert, D., 1999. From ultrasoft pseudopotentials to the projector augmented-wave method. Phys. Rev. B 59, 1758–1775.

Lan, Z., Hu, Y., Qin, W., 2009. Effect of surfactant OPD on the bioleaching of marmatite. Miner. Eng. 22, 10–13.

Li, Y., Kawashima, N., Li, J., Chandra, A.P., Gerson, A.R., 2013. A review of the structure, and fundamental mechanisms and kinetics of the leaching of chalcopyrite. Adv. Colloid Interface 197, 1–32.

Liao, Y., Xu, H., Liu, W., Ni, H., Zhang, X., Zhai, A., Quan, Z., Qu, Z., Yan, N., 2019. One step interface activation of ZnS using cupric ions for mercury recovery from nonferrous smelting flue gas. Environ. Sci. Technol. 53, 4511–4518.

Liu, J., Wang, Y., Luo, D., Chen, L., Deng, J., 2018. Comparative study on the copper activation and xanthate adsorption on sphalerite and marmatite surfaces. Appl. Surf. Sci. 439, 263–271.

Lorenzo-Tallafigo, J., Iglesias-Gonzalez, N., Romero, R., Mazuelos, A., Carranza, F., 2018. Ferric leaching of the sphalerite contained in a bulk concentrate: kinetic study. Miner. Eng. 125, 50–59.

Majuste, D., Ciminelli, V.S.T., Eng, P.J., Osseo-Asare, K., 2013. Applications of in situ synchrotron XRD in hydrometallurgy: literature review and investigation of chalcopyrite dissolution. Hydrometallurgy 131–132, 54–66.

Matsuoka, H., Mitsuhashi, K., Kawata, M., Kato, T., Tokoro, C., Haga, K., Shibayama, A., 2020. Surface properties of copper-sulfide minerals with sodium-hydrosulfide activation. Miner. Eng. 156, 106530.

McIntyre, G.J., Moss, G., Barnea, Z., 1980. Anharmonic temperature factors of zinc selenide determined by X-ray diffraction from an extended-face crystal. Acta Crystallogr. A 36, 482–490.

Mehta, N., Cipullo, S., Cocerva, T., Coulon, F., Dino, G.A., Ajmone-Marsan, F., Padoan, E., Cox, S.F., Cave, M.R., De Luca, D.A., 2020. Incorporating oral bioaccessibility into human health risk assessment due to potentially toxic elements in extractive waste and contaminated soils from an abandoned mine site. Chemosphere 255, 126927.

Meng, X., Zhao, H., Sun, M., Zhang, Y., Zhang, Y., Lv, X., Kim, H., Vainshtein, M., Wang, S., Qiu, G., 2019. The role of cupric ions in the oxidative dissolution process of marmatite: a dependence on Cu^{2+} concentration. Sci. Total Environ. 675, 213–223.

Mezgebe, M.M., Ju, A., Wei, G., Macharia, D.K., Guang, S., Xu, H., 2019. Structure based optical properties and catalytic activities of hydrothermally prepared CuS nanostructures. Nanotechnology 30, 105704.

Mikhlin, Y.L., Kuklinskiy, A.V., Pavlenko, N.I., Varnek, V.A., Asanov, I.P., Okotrub, A.V., Selyutin, G.E., Solovyev, L.A., 2002. Spectroscopic and XRD studies of the air degradation of acid-reacted pyrrhotites. Geochim. Cosmochim. Acta 66, 4057–4067.

Monkhorst, H.J., Pack, J.D., 1976. Special points for Brillouin-zone integrations. Phys. Rev. B 13, 5188–5192.

Ogbughalu, O.T., Vasileiadis, S., Schumann, R.C., Gerson, A.R., Li, J., Smart, R.S.C., Short, M.D., 2020. Role of microbial diversity for sustainable pyrite oxidation control in acid and metalliferous drainage prevention. J. Hazard. Mater. 393, 122338.

Osadchii, E.G., Gorbaty, Y.E., 2010. Raman spectra and unit cell parameters of sphalerite solid solutions ($Fe_xZn_{1-x}S$). Geochim. Cosmochim. Acta 74, 568–573.

Pathak, A., Morrison, L., Healy, M.G., 2017. Catalytic potential of selected metal ions for bioleaching, and potential techno-economic and environmental issues: a critical review. Bioresour. Technol. 229, 211–221.

Perdew, J.P., Burke, K., Ernzerhof, M., 1996. Generalized gradient approximation made simple. Phys. Rev. Lett. 77, 3865–3868.

Qian, G., Fan, R., Short, M.D., Schumann, R., Li, J., Rsc, S., Gerson, A.R., 2018. The effects of galvanic interactions with pyrite on the generation of acid and metalliferous drainage. Environ. Sci. Technol. 52, 5349–5357.

Qiu, T., He, Y., Qiu, X., Yang, X., 2017. Density functional theory and experimental studies of Cu^{2+} activation on a cyanide-leached sphalerite surface. J. Ind. Eng. Chem. 45, 307–315.

Sánchez-Andrea, I., Sanz, J.L., Bijmans, M.F.M., Stams, A.J.M., 2014. Sulfate reduction at low pH to remediate acid mine drainage. J. Hazard. Mater. 269, 98–109.

Sephton, M.G., Webb, J.A., 2019. The role of secondary minerals in remediation of acid mine drainage by Portland cement. J. Hazard. Mater. 367, 267–276.

Shirley, D.A., 1972. High-resolution X-ray photoemission spectrum of the valence bands of gold. Phys. Rev. B 5, 4709–4714.

Simate, G.S., Ndlovu, S., 2014. Acid mine drainage: challenges and opportunities. J. Environ. Chem. Eng. 2, 1785–1803.

Stanton, M.R., Gemery-Hill, P.A., Shanks, W.C., Taylor, C.D., 2008. Rates of zinc and trace metal release from dissolving sphalerite at pH 2.0-4.0. Appl. Geochem. 23, 136–147.

Weisener, C.G., Smart, R.S.C., Gerson, A.R., 2004. A comparison of the kinetics and mechanism of acid leaching of sphalerite containing low and high concentrations of iron. Int. J. Miner. Process. 74, 239–249.

Wetle, R., Bensko-Tarsitano, B., Johnson, K., Sweat, K.G., Cahill, T., 2020. Uptake of uranium into desert plants in an abandoned uranium mine and its implications for phytostabilization strategies. J. Environ. Radioact. 220–221, 106293.

White, S.N., 2009. Laser Raman spectroscopy as a technique for identification of seafloor hydrothermal and cold seep minerals. Chem. Geol. 259, 240–252.

Xie, M., Alsina, M.A., Yuen, J., Packman, A.I., Gaillard, J.F., 2019. Effects of resuspension on the mobility and chemical speciation of zinc in contaminated sediments. J. Hazard. Mater. 364, 300–308.

Yang, B., Zhao, C., Luo, W., Liao, R., Gan, M., Wang, J., Liu, X., Qiu, G., 2020. Catalytic effect of silver on copper release from chalcopyrite mediated by *Acidithiobacillus ferrooxidans*. J. Hazard. Mater. 392, 122290.

Zhang, Y., Zhao, H., Qian, L., Sun, M., Lv, X., Zhang, L., Petersen, J., Qiu, G., 2020. A brief overview on the dissolution mechanisms of sulfide minerals in acidic sulfate environments at low temperatures: emphasis on electrochemical cyclic voltammetry analysis. Miner. Eng. 158, 106586.

Zhang, Y., Zhao, H., Zhang, Y., Liu, H., Yin, H., Deng, J., Qiu, G., 2020b. Interaction mechanism between marmatite and chalcocite in acidic (microbial) environments. Hydrometallurgy 191, 105217.

Zhou, Y., Fan, R., Michael, D.S., Li, J., Russell, C.S., Xu, H., Roger, S.C.S., Andrea, R.G., Qian, G., 2018. Formation of aluminum hydroxide-doped surface passivating layers on pyrite for acid rock drainage control. Environ. Sci. Technol. 11786–11795.

Żmuda-Trzebiatowska, I., Schaefer, K., Sokołowska, A., Rodzik, I., Sobczyk, A.T., Karczewski, J., Śliwiński, G., 2016. Raman investigation of the patina layers on Hungarian copper ingots from a fifteenth century shipwreck. J. Raman Spectrosc. 47, 1528–1533.